Monthly Notices
of the
ROYAL ASTRONOMICAL SOCIETY

MNRAS **489,** 13–27 (2019)
Advance Access publication 2019 July 25

doi:10.1093/mnras/stz2040

An unusual transient following the short GRB 071227

R. A. J. Eyles ,[1]★ P. T. O'Brien,[1] K. Wiersema,[1,2] R. L. C. Starling,[1] B. P. Gompertz,[2] G. P. Lamb ,[1] J. D. Lyman,[2] A. J. Levan,[2,3] S. Rosswog[4] and N. R. Tanvir[1]

[1]*Department of Physics and Astronomy, University of Leicester, University Road, Leicester LE1 7RH, UK*
[2]*Department of Physics, University of Warwick, Coventry CV4 7AL, UK*
[3]*Department of Astrophysics/IMAPP, Radboud University, Nijmegen, The Netherlands*
[4]*The Oskar Klein Centre, Department of Astronomy, AlbaNova, Stockholm University, SE-106 91 Stockholm, Sweden*

Accepted 2019 July 22. Received 2019 July 19; in original form 2019 May 17

ABSTRACT

We present X-ray and optical observations of the short duration gamma-ray burst GRB 071227 and its host at $z = 0.381$, obtained using *Swift*, Gemini South, and the Very Large Telescope. We identify a short-lived and moderately bright optical transient, with flux significantly in excess of that expected from a simple extrapolation of the X-ray spectrum at 0.2–0.3 d after burst. We fit the SED with afterglow models allowing for high extinction and thermal emission models that approximate a kilonova to assess the excess' origins. While some kilonova contribution is plausible, it is not favoured due to the low temperature and high luminosity required, implying superluminal expansion and a large ejecta mass of $\sim$0.1 $M_\odot$. We find, instead, that the transient is broadly consistent with power-law spectra with additional dust extinction of $E(B-V) \sim 0.4$ mag, although a possibly thermal excess remains in the z band. We investigate the host, a spiral galaxy with an edge-on orientation, resolving its spectrum along its major axis to construct the galaxy rotation curve and analyse the star formation and chemical properties. The integrated host emission shows evidence for high extinction, consistent with the afterglow findings. The metallicity and extinction are consistent with previous studies of this host and indicate the galaxy is a typical, but dusty, late-type SGRB host.

Key words: gamma-ray burst: general – gamma-ray burst: individual: GRB 071227.

1 INTRODUCTION

The detection of gravitational wave signal GW 170817 (Abbott et al. 2017), an inspiral and merger of a binary neutron star (BNS) system, coupled with the coincident detection of the short gamma-ray burst (SGRB) GRB 170817A by both the *Fermi Gamma-ray Burst Monitor* (*Fermi-GBM*) and *INTErnational Gamma-Ray Astrophysics Laboratory* (*INTEGRAL*) spacecraft (Goldstein et al. 2017; Savchenko et al. 2017), has greatly strengthened the link between SGRBs and a compact binary progenitor. The merger of two compact objects, either a BNS or a neutron star black hole (NSBH) system, is a cataclysmic event which can power a relativistic jet and an SGRB. This jet, and by extension, the gamma and X-ray emission, is emitted in the direction of the orbital axis of the progenitor system ('on-axis'). SGRBs are conventionally characterized by a T_{90}, the time in which 90 per cent of the prompt emission photons are detected, of less than 2 s and a hard gamma-ray spectrum (Kouveliotou et al. 1993). There is a wide variety in SGRB host galaxies (Leibler & Berger 2010; Fong & Berger 2013). This is in contrast to long gamma-ray bursts (LGRBs), which have a T_{90} greater than 2 s and a softer gamma-ray spectrum, and are linked to highly energetic core collapse supernovae residing in blue star-forming, low-metallicity galaxies (Svensson et al. 2010; Mannucci, Salvaterra & Campisi 2011).

Both short and long GRBs produce broad-band afterglows, which provide a great deal of information about the properties of the jet opening angles, energetics, and circumburst medium (Sari, Piran & Halpern 1999; Piran 2004). Other types of transients are also associated with each type of GRB: for LGRBs, supernovae following the core collapse of their progenitor star (Hjorth et al. 2003), and for SGRBs, kilonovae (e.g. Li & Paczyński 1998; Tanvir et al. 2013; Metzger 2017).

A kilonova is a radioactively powered and rapidly evolving transient, peaking in the optical or NIR depending on time, the progenitor properties, and viewing angle (Metzger 2017). This is due to the behaviour of the different types of ejecta produced during and following the merger process: dynamical and disc wind ejecta (Rosswog 2015). The dynamical ejecta have a varying electron fraction (Y_e) with low Y_e tidally ejected material distributed near the equatorial plane and high Y_e collisional ejecta distributed in a symmetrical sphere at a smaller radius. The disc wind ejecta, similarly to the collisional ejecta, are also distributed in a symmetrical sphere around the merger site but, depending on the neutrino

★ E-mail: raje1@le.ac.uk

winds described later, have a low Y_e and are found at even smaller radii.

The ejecta undergo *r*-process nucleosynthesis (Lattimer & Schramm 1974), with the elements produced varying according to Y_e (Metzger 2017). The neutron-rich equatorial and disc wind material produces heavy lanthanides while the high Y_e material is neutron poor, inhibiting lanthanide production. Decay of the elements produced in this *r*-process nucleosynthesis leads to radioactive heating of the surrounding ejecta and the varying opacities of the ejecta results in the two key components of kilonova emission: ∼week long red infrared around the equator and more isotropically distributed ∼day long blue optical emission, respectively. Following a typical SGRB, it would be expected that the on-axis viewing angle would mean that it is the blue component that would primarily be observed assuming it is not outshone by the SGRB afterglow itself, although it is also likely the red component would be observable as the viewing cone is broad. Depending on the masses and types of the progenitors, it is also possible for a magnetar central engine to form which produces a neutrino wind, increasing the Y_e of the nearby disc wind ejecta. The additional energy injected by this magnetar, as well as the higher Y_e of the disc wind ejecta, leads to a longer lived kilonova with bluer emission lasting several hours to days (Kasen, Fernández & Metzger 2015). In addition to these components, it has been proposed that kilonovae may be preceded by precursor emission peaking in the ultraviolet. Directly following the merger, the fastest ejecta can form an outer layer composed primarily of 'free' neutrons. These free neutrons inject additional energy into the ejecta, heating the material and intensifying the emission produced (Metzger et al. 2015).

Observational constraints on the diversity of kilonova behaviour are very limited (Gompertz et al. 2018). For instance, it is believed that a kilonova was detected following GRB 130603B (Tanvir et al. 2013), but this was limited to a single data point deviating from the underlying afterglow light curve. A number of other kilonova candidates are briefly discussed in comparison to GRB 071227 in Section 3.2.2.

The best example to date of a kilonova signature was the emission associated with the gravitational wave event GW 170817. The accompanying optical and infrared kilonova AT 2017gfo, has been observed in exquisite detail (e.g. Abbott et al. 2017; Covino et al. 2017; Cowperthwaite et al. 2017; Kilpatrick et al. 2017; Smartt et al. 2017; Tanvir et al. 2017). This has allowed a much more thorough investigation into the resultant kilonova than has previously been possible. Both the red and blue emission can be seen which, along with the SGRB energetics and gravitational wave data, implies the kilonova is being viewed off-axis. The highly sampled light curves resulting from observations of AT 2017gfo also allow the temporal evolution of kilonova emission to be more accurately modelled (e.g. Gompertz et al. 2018).

There are only a few short bursts for which well-sampled multi-wavelength afterglows are available. These observables can be used to determine useful information on the properties of the progenitors and in turn allow the inference of global rates and properties of SGRBs. However, this is still a relatively small sample of SGRBs. GW 170817 has also prompted the evaluation of potential kilonovae in past SGRBs (Gompertz et al. 2018; Ascenzi et al. 2019; Jin et al. 2019; Lamb et al. 2019; Rossi et al. 2019; Troja et al. 2019). In this paper, we aim to bring the short GRB 071227 into both these catalogues.

GRB 071227 is a relatively well-studied example of an SGRB. In particular, D'Avanzo et al. (2009) is a notable counterpart to this paper, presenting optical photometry of the GRB and photometric and spectroscopic analysis of the host as we do here. Their observations were performed using the FOcal Reducer and low dispersion Spectrograph (FORS2) instrument on the Very Large Telescope (VLT). They found GRB 071227 to be a fairly typical SGRB although they only had one observation during the afterglow phase. We revisit these observations in this paper and use them to obtain deeper upper limits than previously and in addition, we include new deep multiband Gemini South observations. D'Avanzo et al.'s spectroscopic observations of the host provided a redshift of 0.381, a star formation rate of 0.6 $M_\odot$ yr^{-1}, and a metallicity of $12 + \log(O/H) = 8.2$–8.8 dex. Additional optical and NIR photometry is found in D'Avanzo et al. (2007), Berger, Morrell & Roth (2007), and Nicuesa Guelbenzu et al. (2012).

Nicuesa Guelbenzu et al. (2014) also analysed the host galaxy, presenting radio observations as well as identifying a *Wide-field Infrared Survey Explorer* (*WISE*) counterpart. Using spectral energy distribution (SED) models, they derive a star formation rate of ∼24 $M_\odot$ yr^{-1}. The contrast with D'Avanzo et al. (2009)'s results is suggested to be due to high optical extinction in the host. Further SED analysis is also presented by Leibler & Berger (2010) who measure stellar population ages. The host morphology is investigated in Fong & Berger (2013).

GRB 071227 has also been evaluated as a GRB with extended emission (EE; Gompertz, O'Brien & Wynn 2014; Lien et al. 2016; Gibson et al. 2017), finding it to fit well with a magnetar propeller model, while Kisaka, Ioka & Sakamoto (2017) found evidence of both extended and plateau emission, and has been investigated in relation to X-ray flares in SGRBs (Margutti et al. 2011), in which a flare was identified in the first 200 s following the GRB. Finally, GRB 071227 is in the sample examined by Rossi et al. (2019) for kilonova signatures by comparison with AT 2017gfo, finding that any kilonova is likely several times dimmer than the afterglow.

In this paper, we report our own optical photometry obtained using the Gemini Multi-Object Spectrograph instrument (GMOS-S) at the Gemini South observatory, finding, at a time of ∼0.26 d, apparent excess optical flux when compared with a synchrotron afterglow model extrapolation of the X-ray emission. We investigate the scenarios that could lead to this apparent excess, including kilonovae and reverse shocks. We also add further spectroscopic observations and analysis thereof of the host. In Section 2, we summarize our Gemini South observations and processing as well as the available data from the *Neil Gehrels Swift Observatory*, hereafter *Swift*, satellite and the VLT. Section 3 deals with the properties of the X-ray and optical transients and our investigation into the mechanisms that could have produced them, while Section 4 examines the properties of the host galaxy. Section 5 presents our conclusions.

Throughout this paper we adopt a cosmology with $H_0 = 71\ km\ s^{-1}\ Mpc^{-1}$, $\Omega_m = 0.27$, and $\Omega_\Lambda = 0.73$. A redshift of $z = 0.381$ therefore corresponds to a luminosity distance of 2039.0 Mpc, and 1 arcsec corresponds to 5.4 kpc. Hereafter we use the notation $F \propto t^{-\alpha}\nu^{-\beta}$, where α and β are the temporal and spectral power-law indices, respectively. In the case of spectral fits performed using XSPEC, our errors are 90 per cent confidence. All other errors are given to 1σ.

2 OBSERVATIONS AND DATA REDUCTION

2.1 *Swift* observations

Swift was triggered at 20:13:47 UT and slewed to the burst at RA $03^h52^m29^s$, Dec. $-55^d57^m08^s$ (Sakamoto et al. 2007a). The prompt light curve indicated multiple peaks during a T_{90} of 1.8 ± 0.4 s (Sakamoto et al. 2007b). However, a more careful

Table 1. Log of Gemini South observations. All magnitudes are *AB* and corrected for Galactic extinction. The upper limits are 3σ.

Epoch	Time started (UT)	Mean time after burst (d)	Exposure time (s)	Filter/grism	Seeing (mean FWHM in arcsec)	Mean airmass	OT magnitude
1	2007 Dec 28 00:56:58	0.27119	20 × 180	*r*	1.75	1.16	24.03 ± 0.04
		0.26675	10 × 180	*i*	1.56	1.11	23.26 ± 0.04
		0.23900	10 × 180	*z*	1.54	1.11	22.47 ± 0.07
2	2008 Jan 1 02:06:37	4.30379	20 × 180	*r*	0.86	1.19	$\geqq 26.72$
		4.32089	10 × 180	*i*	0.77	1.20	$\geqq 25.23$
		4.29318	10 × 180	*z*	0.71	1.15	$\geqq 24.10$
3	2008 Jan 4 05:08:14	7.39899	20 × 180	*r*	0.97	1.54	$\geqq 26.85$
		7.43925	3 × 180	*i*	0.92	1.78	–
		7.43092	3 × 180	*z*	1.48	1.86	–
4	2008 Jan 11 02:40:48	14.29787	20 × 180	*r*	0.98	1.21	–
5	2008 Jan 17 00:56:21	20.19667	1830	GG455_G0329 / R400	0.77	1.11	Spectrum

Table 2. Log of VLT/FORS2 observations. All observations used the ESO *R_Special* filter. All magnitudes are *AB* and corrected for Galactic extinction. The upper limits are 3σ.

Epoch	Time started (UT)	Mean time after burst (d)	Exposure time (s)	Mean seeing (arcsec)	Mean airmass	OT magnitude
1	2007 Dec 28 03:08:37	0.29055	2 × 120	0.7	1.20	24.17 ± 0.12
2	2007 Dec 31 05:05:38	3.37133	3 × 180	0.7	1.46	$\geqq 25.39$
3	2008 Jan 3 02:30:56	6.26790	5 × 180	0.8	1.19	$\geqq 24.83$
4	2008 Jan 7 02:02:10	10.24790	5 × 180	0.8	1.18	$\geqq 25.01$
5	2008 Jan 16 05:16:31	19.38287	5 × 180	0.7	1.84	$\geqq 25.23$
6	2008 Jan 18 01:58:14	21.25139	10 × 180	0.8	1.22	$\geqq 25.32$
7	2008 Jan 23 02:12:35	26.21775	10 × 180	0.9	1.19	–
8	2008 Feb 6 02:12:35	40.26121	10 × 180	1.1	1.41	–

reduction revealed a lengthy extended emission period following the burst, in common with some other SGRBs. If accounted for, the extended emission increases the T_{90} estimate considerably to 142.5 ± 48.4 s (Lien et al. 2016). In the *Swift*-BAT bandpass, $E_{\gamma,\mathrm{iso}}$ is $1.96^{+0.30}_{-0.29} \times 10^{50}$ erg.

We retrieved the X-Ray Telescope (XRT) data from the UK *Swift* Science Data Centre (UKSSDC)[1] and corrected it for line-of-sight absorption using the ratio of counts-to-flux unabsorbed to counts-to-flux observed from the fit to the late-time photon counting mode spectrum on the UKSSDC. This is a factor of 1.02.

2.2 GMOS-S imaging

Optical observations were performed at Gemini South using the GMOS-S (Hook et al. 2004). These observations were performed using the original EEV CCDs, with an unbinned pixel size of 0.073 arcsec. In this case, 2 × 2 binning was used, hence our pixel size is 0.146 arcsec. The *r*, *i*, and *z* filters used in GMOS-S are based on those used in the Sloan Digital Sky Survey as presented in Fukugita et al. (1996). Conditions during the observations were generally good, although seeing during the first epoch was notably poorer (see Table 1).

We reduced the data using the GEMINI IRAF package, specifically the GMOS subpackage. The method used is based on that found in the GMOS Data Reduction Cookbook (Shaw 2016). Master bias and flat frames were constructed for each filter using the available observations closest to each epoch and were then applied to the raw science frames. There was significant fringing present in the raw *i* and *z* frames, a common problem for images taken using the older EEV CCDs. Typically, the fringing is removed using master fringe frames taken once per semester. However, this was found to be ineffective in this case and instead we constructed fringe frames from the science frames using the GIFRINGE task. These were found to be much more effective at minimizing the fringing present in the *i* and *z*. As there was no apparent fringing in the *r* frames, no correction was applied. The data from the individual CCDs were then mosaicked together to create an image of the entire field. The median value of the data was substituted into any blank pixels, such as those in the gaps between the CCDs.

We combined the individual images using IRAF tasks SHIFTADD[2] and IMCOADD, with the final output being the mean of the stack. We used the GAIA software (Draper et al. 2014) to produce a final world coordinate system (WCS) calibration for each image manually using 49 USNO-B objects in the field and derived a photometric calibration for each stacked frame by matching stars to the SkyMapper catalogues (Wolf et al. 2018).

We used the HOTPANTS code (Becker 2015) for image subtraction, a reimplementation of the ISIS algorithm (Alard 2000). This uses a space-varying kernel method to achieve effective subtraction across the entire field by matching point spread functions (PSFs) between images. The last epoch observed for each filter were taken as the template images, i.e. epoch 4 for *r* and epoch 3 for *i* and *z*. The subtraction for epoch 1 in the *r* band is shown in Fig. 1.

[1] http://www.swift.ac.uk/index.php

[2] Developed by E. Rol.

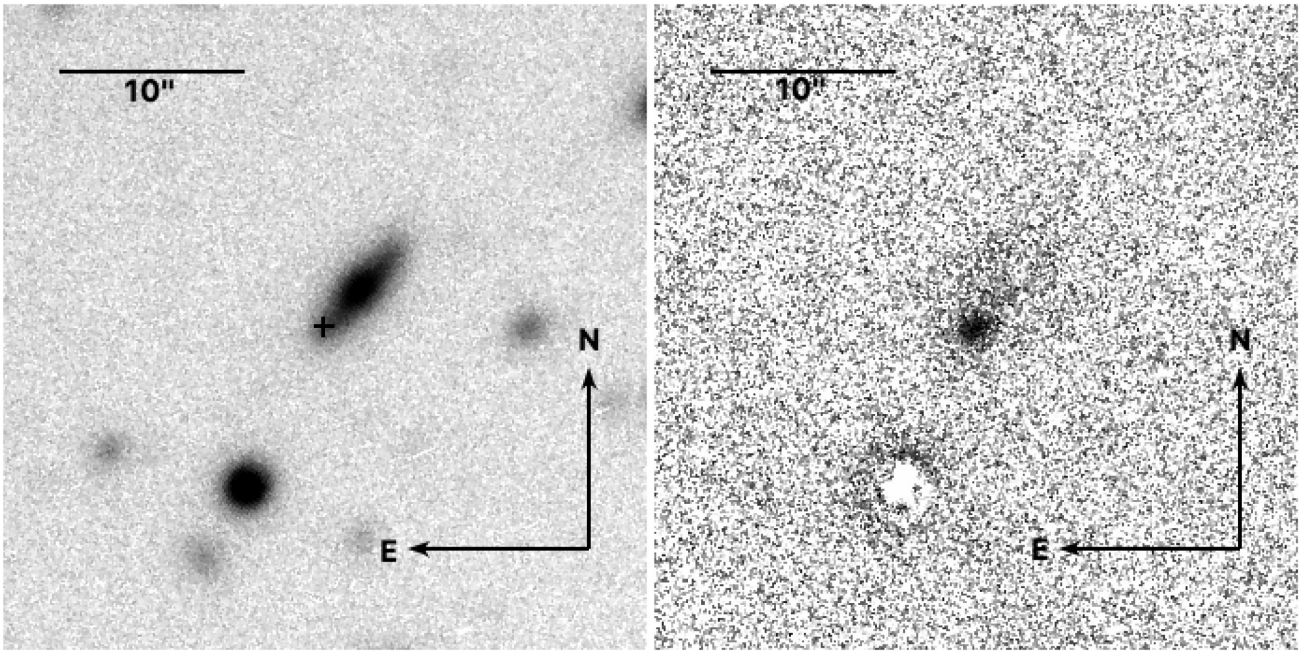

Figure 1. The observed field near GRB071227 in epoch 1 in the *r* filter (left) and the same field with epoch 4 subtracted (right), demonstrating the fading optical transient. The cross in the left image indicates the position of the transient in the host. A subtraction artefact (the residual from a bright star) is also visible below the residual from the transient.

2.3 VLT/FORS2 imaging

As previously mentioned, we have reanalysed the VLT data examined in D'Avanzo et al. (2009). Observations were performed using the *R_Special* filter (ESO 2018) on the FORS2 instrument, which has an unbinned pixel size of 0.125 arcsec. Again, 2 × 2 binning was used leading to a pixel size of 0.25 arcsec. The data were obtained from the European Southern Observatory archive.[3]

We processed the data using the standard EsoReflex workflow for the FORS instruments (Freudling et al. 2013) then stacked the individual frames using IMCOADD as described above. Photometric calibrations were again evaluated by comparison with the SkyMapper catalogue (Wolf et al. 2018), calibrating directly to the *r* band. Image subtraction was performed using HOTPANTS, again taking the final epoch, in this case epoch 8, as the template image. It should be noted that we were unable to achieve an effective subtraction for epoch 7, likely due to this image being of lower quality and HOTPANTS therefore being unable to accurately match the PSFs.

2.4 GMOS-S spectroscopy

To further characterize the host galaxy, we obtained a spectrum with GMOS-S using the nod and shuffle technique, which increases signal to noise at the red end by increasing accuracy of skyline subtraction (see Glazebrook & Bland-Hawthorn 2001 for a description of the technique) and suppresses the effects of the severe fringing of the GMOS-S detectors. The 1.0 arcsec wide slit was oriented along the major axis of the galaxy (sky position angle 140 deg, see Fig. 2), in contrast to D'Avanzo et al. (2009) who oriented their slit North to South centred on the nucleus of the host. We used low-resolution grism R400 and the GG455_G0329 filter, resulting in a

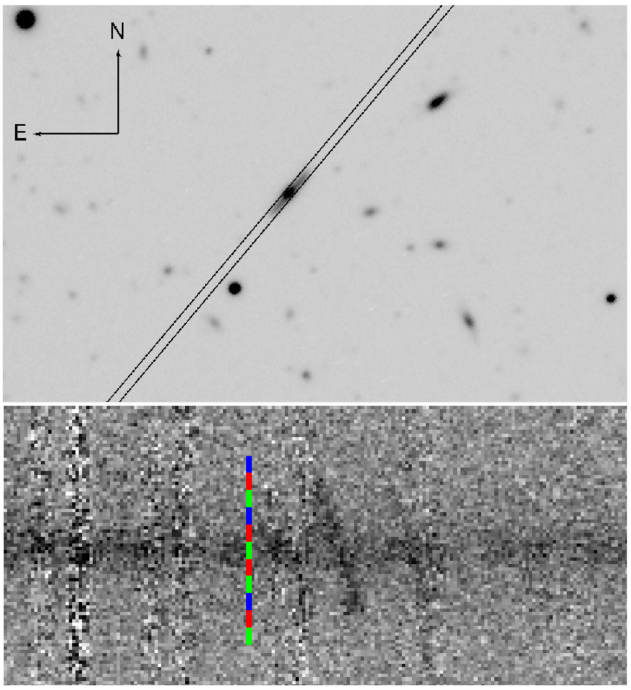

Figure 2. The orientation of the 1.0 arcsec wide GMOS-S slit, 140 deg parallactic angle, is indicated on the second epoch *r* image (top) and a small part of the two-dimensional spectrum centred on the Hα emission line (bottom). Redwards (right) of the Hα line the, much fainter, [N II] λ6585 line is visible. The total aperture consisting of 11 subapertures of each 5 pixels is indicated. The noisy vertical stripes perpendicular to the trace of the galaxy are low amplitude residuals from the skyline subtraction through the nod and shuffle technique.

[3] http://archive.eso.org/cms.html

wavelength range of ∼5500–9290 Å (with a central wavelength of ∼7200 Å). 30 nod and shuffle cycles were used and the total net exposure time was 1830 s. An atmospheric dispersion compensator was used to minimize colour dependent slit losses. The data were reduced using the standard nod and shuffle procedures in the GEMINI package in IRAF, and tasks in the SPECRED package were used for extraction.

We extracted the host galaxy spectrum by using the relatively bright continuum of the bulge to fit the shape of the trace, then extracted 11 adjoining, equally sized subapertures following this trace. The subapertures are 5 pixels in size, corresponding to 0.73 arcsec per subaperture, i.e. a value broadly matched to the seeing full width at half-maximum (FWHM). This corresponds to a physical scale of 3.9 kpc per subaperture. The GRB location falls in subaperture 2. The spectra extracted from each subaperture are referred to as subspectra hereafter. The subspectra were wavelength calibrated using a CuAr lamp spectrum and the dispersion solution had an rms of 0.3 Å. From the FWHM of a Gaussian fit on the arc lines, we measured a nominal spectral resolution of 6.9 Å, corresponding to 280 km s^{-1} at 7300 Å.

Flux calibration of the subspectra was done using observations of the spectrophotometric standard star Hiltner 600 (Hamuy et al. 1992; Hamuy et al. 1994), taken under photometric conditions. Atmospheric extinction correction was done by applying the average CTIO atmospheric extinction curve. As the effective airmass was low, the effects of the atmospheric extinction correction were negligible. A Galactic dust extinction correction was performed by using the $E(B-V)$ value of 0.013 mag (Schlegel, Finkbeiner & Davis 1998), assuming a Galactic extinction law A_λ/A_V expressed as $R_V = A_V/E(B-V)$ (Cardelli, Clayton & Mathis 1989). We made the standard assumption $R_V = 3.1$ (Rieke & Lebofsky 1985).

3 PROPERTIES OF THE TRANSIENT

3.1 Broad-band light curve

The *Swift* XRT identified an X-ray transient at RA 03$^{\rm h}$52$^{\rm m}$31$^{\rm s}$.21, Dec. −55$^{\rm d}$59$^{\rm m}$03$^{\rm s}$.1 (Beardmore, Page & Sakamoto 2007). The XRT light curve, as shown in black in Fig. 3 and red in Fig. 4, is well fitted with a double broken power law between 210 s and 34.8 ks. This fit has parameters $\alpha_1 = 1.1 \pm 0.2$, $t_{\rm break_1} = 183 \pm 7$ s, $\alpha_2 = 5.3^{+1.2}_{-0.6}$, $t_{\rm break_2} = 389 \pm 65$ s, and $\alpha_3 = 1.1 \pm 0.2$ (Beardmore et al. 2007; Evans et al. 2007, 2009). When compared to most *Swift* detected SGRBs, as shown in Fig. 4, the XRT light curve is found to be slightly underluminous, particularly at later times, but is not atypical.

We used SEXTRACTOR 2.19.5 (Bertin & Arnouts 1996) to detect and extract sources from our optical data to a 5σ confidence threshold. Using the first epoch *r*-band difference image, we identified an optical transient which had an *AB* magnitude of 24.03 ± 0.03 at a position of RA 03$^{\rm h}$52$^{\rm m}$31$^{\rm s}$.25, Dec. −55$^{\rm h}$59$^{\rm m}$02$^{\rm s}$.87 (J2000) with an uncertainty of 0.28 arcsec dominated by the rms of the astrometric solution of the USNO stars used for the WCS calibration. This is consistent with the positions of the X-ray and optical transients found by Beardmore et al. (2007) and D'Avanzo et al. (2009), respectively. The transient is also detected in the first epoch *i*- and *z*-band images at *AB* magnitudes 23.26 ± 0.04 and 22.47 ± 0.07, respectively.

The optical transient is not detected in subsequent epochs, however, indicating its fading. We identified upper limits for these later epochs by injecting artificial sources into the input image and performing subtraction to identify where the magnitude error reached the 3σ threshold. The detected magnitudes and upper limits from our GMOS-S observations are summarized in Table 1.

This rapid fading can also be identified in our analysis of the VLT/FORS2 data as summarized in Table 2. Again, the transient was only identified in the first epoch, at an *R*-band *AB* magnitude of 24.17 ± 0.12, and we therefore again used injected artificial sources in the later epochs to evaluate deeper upper limits than those identified by D'Avanzo et al. (2009). As we were unable to obtain an effective subtraction, we do not have an upper limit for epoch 7. Fitting our detections and upper limits with power laws indicated minimum temporal decay indices of $\alpha_r \gtrsim 0.87$, $\alpha_i \gtrsim 0.65$, and $\alpha_z \gtrsim 0.52$ for the *r*, *i*, and *z* bands, respectively.

3.2 Broad-band spectral energy distribution (SED)

We used XSPEC 12.10.0 (Arnaud 1996; Dorman & Arnaud 2001) from HEASOFT 6.24 to evaluate the broad-band SED. Full details on the models used and our fitted parameters are presented in Appendix A. We first fitted the X-ray and optical data separately. An absorbed power-law model was used to fit the XRT spectrum at a mean time in log space coincident to the first optical GMOS-S epoch, 21 635 s after the burst, finding a photon index, $\Gamma = \beta + 1$, of $1.58^{+0.87}_{-0.57}$ and host intrinsic column density upper limit of $N_H \leqq 2.97 \times 10^{21}$ cm^{-2} in addition to the fixed Galactic column density of $N_H = 1.31 \times 10^{20}$ cm^{-2} (Willingale et al. 2013; see Table A1 for full details). This fit has a reduced chi-squared of 1.130. The parameters identified agree with those found by *Swift*'s automatic fitting algorithms (Evans et al. 2009) and are consistent with the broader sample of SGRBs (D'Avanzo et al. 2014; Fong et al. 2015).

Both the light curve and spectral properties of the X-ray data are consistent with a typical afterglow model synchrotron emission from a relativistic blast wave (Sari & Piran 1999; Sari et al. 1999). The photon index and the temporal slope (α_3 at this time) can be used to independently evaluate the electron energy distribution index, *p*, using the standard closure relations (Sari, Piran & Narayan 1998; Chevalier & Li 1999, 2000; Granot & Sari 2002)

$$p(\Gamma) = \begin{cases} 2\Gamma - 1 = 2.16^{+1.74}_{-1.14} & \text{for} \nu_{\rm m} < \nu < \nu_{\rm c} \\ 2(\Gamma - 1) = 1.16^{+1.74}_{-1.14} & \text{for } \nu_{\rm m} < \nu_{\rm c} < \nu \end{cases} \quad (1)$$

$$p(\alpha, k) = \begin{cases} \frac{4\alpha+3}{3} = 2.47 \pm 0.27 & \text{for } \nu_{\rm m} < \nu < \nu_{\rm c} \text{ and } k = 0 \\ \frac{4\alpha+1}{3} = 1.80 \pm 0.27 & \text{for } \nu_{\rm m} < \nu < \nu_{\rm c} \text{ and } k = 2 \\ \frac{2(2\alpha+1)}{3} = 2.13 \pm 0.27 & \text{for } \nu_{\rm m} < \nu_{\rm c} < \nu \text{ and any } k \end{cases}, \quad (2)$$

where $\nu_{\rm m}$ is the peak frequency, $\nu_{\rm c}$ is the cooling frequency, and *k* describes the particle number density of the surrounding medium as a function of radius, $n(r) \propto r^{-k}$, although it should be noted that a wind like density profile is not expected following a neutron star merger, hence *k* is expected to be 0 (Chevalier & Li 1999). We do not include energy injection which is thought to be responsible for the unusual features observed in a subset of SGRB light curves (e.g. Gompertz et al. 2014). Together, these imply $2.1 \lesssim p \lesssim 2.4$ in the regime $\nu_{\rm m} < \nu < \nu_{\rm c}$, consistent with the results of Fong et al. (2015) where they found $p = 1.92 \pm 0.31$ for this burst and a mean value of *p* of $2.43^{+0.36}_{-0.28}$ for their full population of SGRBs.

XSPEC was also used to fit our first GMOS-S optical epoch. Because the mean time of our *z*-band observation was somewhat earlier than the other bands, we extrapolated the flux density to

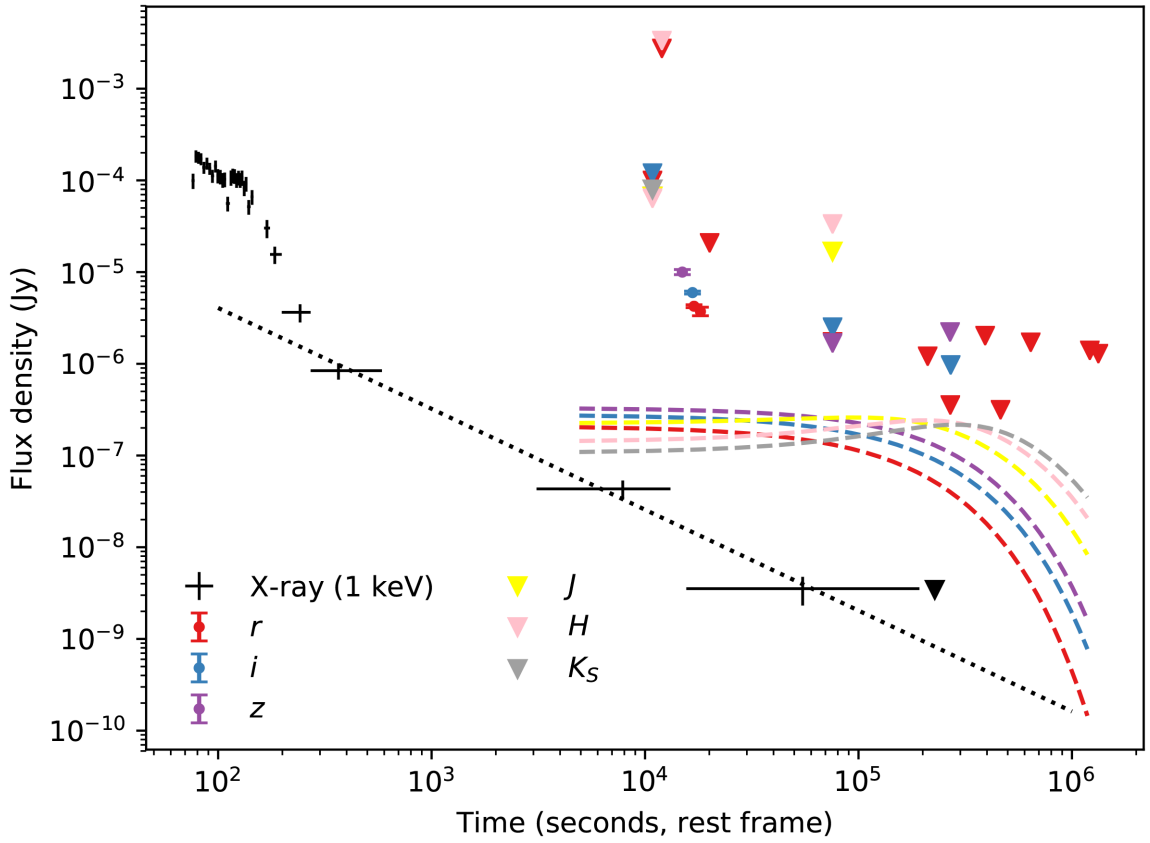

Figure 3. The broad-band light curve of GRB 071227. Extinction corrections of $N_H = 2.97 \times 10^{21}$ cm^{-2} and $E(B-V) = 0.43$ mag have been applied. Our *Swift* and optical data are supplemented by additional optical and NIR photometry from GROND (Nicuesa Guelbenzu et al. 2012), REM (D'Avanzo et al. 2007), and Magellan (Berger et al. 2007). Triangles represent 3σ upper limits and the black dotted line indicates the slope of $\alpha = 1.1$ followed in the X-ray. Models of the kilonova AT 2017gfo light curves (Gompertz et al. 2018), extrapolated to the redshift of GRB 071227, are shown in the dashed lines.

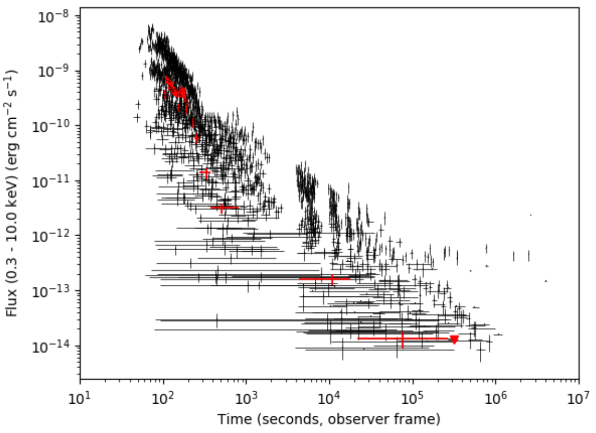

Figure 4. The available XRT light curves for the SGRBs in the catalogue presented in Fong et al. (2015) in black with GRB 071227 highlighted (red).

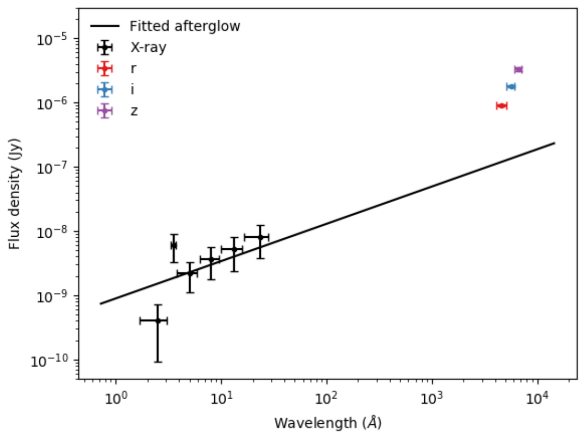

Figure 5. The X-ray only afterglow fit extrapolated to optical wavelengths demonstrating the apparent optical excess.

this time assuming a power-law decay with temporal decay index of 1.1, consistent with that inferred from the X-ray light curve. We again used an absorbed power-law model to find $\Gamma \sim 4.49$ with no host extinction contribution assumed (see Table A2 for full details). While this is somewhat unconstrained due to only having three data points available, this is still a surprising result, as the optical spectrum is typically shallower than the X-ray at this time. It also implies a much higher electron energy distribution index than typically found in GRBs (∼7–8 depending on the regime assumed). Extrapolating the power law derived from the X-ray SED to optical wavelengths, as shown in Fig. 5, also indicates that the optical flux is underestimated, even when the effects of optical extinction have not been removed. Below, we consider several possibilities for the apparent discrepancy.

3.2.1 An afterglow explanation for the apparent optical excess

It is possible that the optical and X-ray transients are indeed consistent with a single afterglow model. We therefore attempted to fit both the X-ray and optical data together using XSPEC to gain a better picture of the varying situation between these wavelengths. Again, an absorbed power-law model was used, this time a combination of both the X-ray and optical models. A pair of power-law fits with a reduced chi-squared of 1.113 and the same photon index of $1.58^{+0.56}_{-0.57}$ were found, which required both a high optical extinction ($E(B-V) \sim 0.85$) and the normalization of the optical to be ∼140 times larger than that of the X-ray (see Table A3 for full details), with any single normalization fit being extremely poor. This level of extinction is plausible in the host, as we find in Section 4.2, but the large difference in the normalization is still problematic.

Due to limitations within XSPEC (the large wavelength difference between our X-ray and optical data and the greater amount of X-ray data meaning any fit is naturally weighted towards fitting best with the X-ray), we used a Markov Chain Monte Carlo (MCMC) method to better evaluate the afterglow. The X-ray data were rebinned and the errors of our X-ray only fit were used to define our fit parameter space. We first assumed that the N_H and A_V were related by $N_H = (2.21 \pm 0.09) \times 10^{21} A_V$, as identified by Güver & Özel (2009) for the Galaxy. Our fitted parameters therefore were the slope and normalization of the afterglow and the N_H with $E(B-V)$ derived from the relation above. Assuming $R_V = 3.1$ as in the Galaxy, this identified a fit to a Γ of $2.19^{+0.06}_{-0.04}$ at a reduced chi-squared of 2.501, where $N_H = 2.97^{+0.01}_{-0.64} \times 10^{21}$ cm^{-2} and $E(B-V) = 0.43^{+0.01}_{-0.09}$ mag (see Table A4 for full details), as shown in Fig. 6 (top). Using other values of R_V, such as 2.93 and 3.16 as found in the Small and Large Magellanic Clouds (SMC and LMC), respectively, has an insignificant effect on this fit. The extinction corrections identified in this fit have been applied in Fig. 3.

In a number of GRBs, the relation between N_H and A_V above is not obeyed, however, likely due to a dust-to-gas ratio in the host that differs from that of the Milky Way (e.g. Li, Li & Wei 2008a; Li et al. 2008b). We therefore also fitted our SED allowing $E(B-V)$ to vary independently of N_H, as shown in Fig. 6 (bottom). This identified a fit to a Γ of $2.15^{+0.01}_{-0.06}$, where $N_H = 2.77^{+5.51}_{-2.77} \times 10^{20}$ cm^{-2} and $E(B-V) = 0.45^{+0.01}_{-0.07}$ (see Table A5 for full details). This fit has a reduced chi-squared of 3.094, an increase likely due to the extra parameter being fitted. This result possibly implies a high dust-to-gas ratio in the host relative to the Milky Way, but could also indicate that the fit is relatively insensitive to N_H.

The above fits both still result in a z-band excess, but are generally consistent within errors and are also consistent with the results from *Swift*'s automatic fitting. Returning to the electron energy distribution index, we find that for the first of our MCMC fits, where N_H and A_V are related as in the Galaxy, that

$$p(\Gamma) = \begin{cases} 2\Gamma - 1 = 3.38^{+0.12}_{-0.08} & \text{for } \nu_m < \nu < \nu_c \\ 2(\Gamma - 1) = 2.38^{+0.12}_{-0.08} & \text{for } \nu_m < \nu_c < \nu\,. \end{cases} \quad (3)$$

This, together with our analysis of p in relation to α above, still indicates that $2.1 \lesssim p \lesssim 2.4$, but in the regime $\nu_m < \nu_c < \nu$. This result is also still consistent with the findings of Fong et al. (2015).

3.2.2 A kilonova explanation for the apparent optical excess

An alternate and possibly the more obvious source for apparent excess flux at optical or IR wavelengths following a short GRB is thermal emission arising from a kilonova. However, we find this to be somewhat problematic in the case of GRB 071227. Taking our X-ray only fit (Γ ∼ 1.58) to be representative of the afterglow, fitting the remaining excess with no reddening assumed to a thermal blackbody model yields a low temperature (∼3600 K) but a high luminosity (∼1.3×10^{43} erg s^{-1}) that require a superluminal expansion velocity according to the Stefan–Boltzmann law.

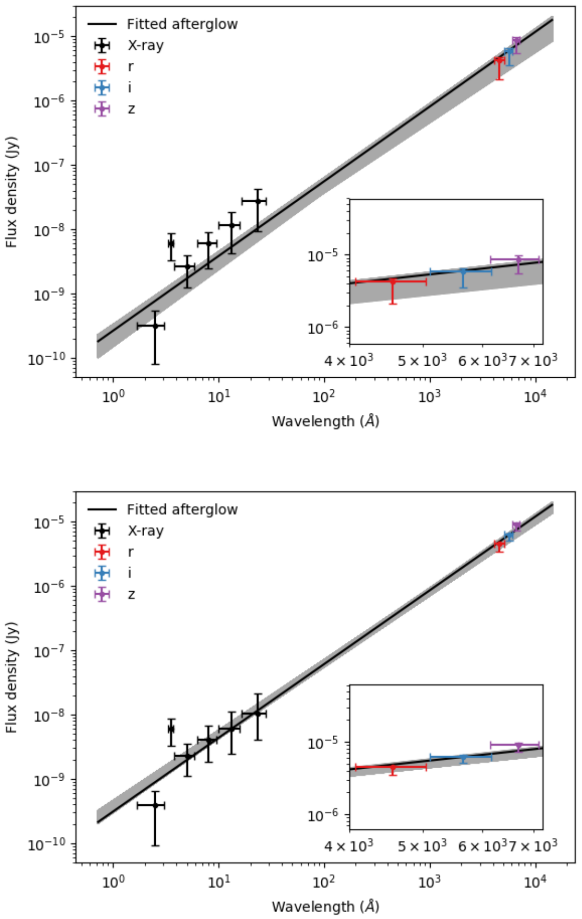

Figure 6. Our afterglow fits obtained using an MCMC method where N_H and A_V are linked by the relation identified by Güver & Özel (2009) (top) and where they are free to vary independently (bottom). The shaded regions indicate the 1σ errors on our fits.

The ejecta mass required for such a luminosity is also somewhat problematic in itself. Simply scaling the luminosity inferred from AT 2017gfo implies an ejecta mass following GRB 071227 of ∼0.2 $M_\odot$, double the approximate maximum expected for a BNS merger of ∼0.1 $M_\odot$ (Metzger 2017).

Alternatively, we can directly estimate the ejecta mass by inspecting nuclear heating rates. Using the Finite Range Droplet Model (FRDM; Möller et al. 1995) for the nuclear masses, network calculations indicate a nuclear heating rate of ∼10^{11} erg g^{-1} s^{-1} at 0.26 d (Korobkin et al. 2012). Making the extreme assumption that all released energy is observed as radiation yields a lower limit on the ejecta mass of 0.09 $M_\odot$. By applying a more realistic efficiency of ∼0.6 (e.g. fig. 8 in Rosswog et al. 2017), however, indicates a mass closer to the ∼0.2 $M_\odot$ found above. It is also important to realize that the nucleosynthesis path for the very low electron fractions of a neutron star merger meanders through largely unknown nuclear territory close to the neutron dripline where no experimental information is available. Theoretical nuclear mass

formulae that equally well reproduce known nuclear data therefore can yield substantially different heating rates. For example, very low Y_e trajectories produce substantially different amounts of nuclei in the translead region ($A > 200$) depending on whether, for instance, the FRDM mass model or the Duflo–Zuker mass formula (DZ31; Duflo & Zuker 1995) are employed. As a result, the effective heating rates at time-scales of days can differ by factors of a few (Barnes et al. 2016; Rosswog et al. 2017). Making the most optimistic assumptions, namely that the ejecta are dominated by very low Y_e material and the nuclear heating is close to the DZ31 mass formula values, the total ejecta mass may be brought down below $\sim 0.1\ M_\odot$. Such large values can in principle be ejected in some NSBH mergers for favourable parameter combinations (mass ratio, neutron star compactness, black hole spin) (Rosswog 2005; Foucart et al. 2014; Brege et al. 2018), but not all NSBH mergers are expected to eject such large masses (e.g. Foucart et al. 2019). In summary, the large required mass may be ejected in an NSBH merger, but it may require a collusion of number of parameters and therefore, while in principle possible, is not our preferred interpretation.

There are two other mechanisms that could reduce the ejecta mass required, a 'free' neutron precursor (Metzger 2017) or a trapped jet leading to a bright thermally emitting relativistic cocoon peaking at optical wavelengths (Kasliwal et al. 2017). However, a UV precursor is inconsistent with the much redder temperatures observed here, while the gamma-ray and X-ray data both show no indication of such a trapped jet, in which case any jet heating is too inefficient to produce the high luminosity seen here (Duffell et al. 2018).

Although this fit is unsuccessful, the errors on our afterglow and optical extinction expand the available parameter space. Varying the afterglow and extinction and refitting the excess therefore provides a more thorough investigative tool into the possibility of this excess being the result of a kilonova. For a given temperature, the luminosity of a kilonova is limited such that the expansion velocity remains below c. This is given by

$$L < 4\pi c^2 t^2 \sigma T^4, \tag{4}$$

where t is the time since the merger in the rest frame and σ is the Stefan–Boltzmann constant. Along with assuming a maximum ejecta mass of $0.1\ M_\odot$, an r-process heating rate of $\sim 10^{11}$ erg s^{-1} g^{-1} as derived using the FRDM and an observed temperature range of 3000–20 000 K, this defines our expected kilonova parameter range, shown in Fig. 7. Also shown in Fig. 7 in grey-scale are the parameters inferred by fitting blackbodies to the optical excess as the extinction, normalization, and slope of the afterglow power law are varied within the full range of the 90 per cent errors inferred by our X-ray only fit. We again used the relation identified by Güver & Özel (2009) to infer an upper limit to the optical extinction of $E(B - V) \sim 0.45$ from the fitted N_H upper limit.

The continued lack of agreement between these fits and the plausible parameter space of our kilonova is clear and strongly indicates that the optical excess following GRB 071227 is not primarily the result of a kilonova and is instead likely dominated by afterglow. A thermal contribution is still plausible, however, which could be responsible for the small excess still apparent in the z band of our afterglow fits and it is therefore useful to compare the properties of GRB 071227 with several kilonova candidates: GRBs 050709 (Fox et al. 2005; Hjorth et al. 2005; Jin et al. 2016), 080503 (Perley et al. 2009; Metzger & Fernández 2014; Metzger & Piro 2014), 130603B (Tanvir et al. 2013), and 150101B (Fong et al. 2016; Troja et al. 2018). Other candidates include GRBs 070809 (Jin et al. 2019) and 160821B (Lamb et al. 2019; Troja et al. 2019), although these are more recently identified and therefore not examined in detail here.

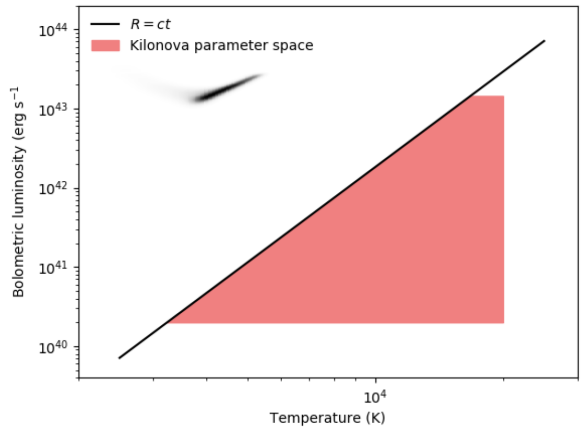

Figure 7. The approximate parameter space open to kilonovae (light red) where the maximum luminosity at lower temperatures is defined by the maximum radius to which the ejecta velocity can expand by the time of our first optical epoch (black line). The grey-scale indicates the range of our blackbody fits as the afterglow parameters and optical extinction are varied.

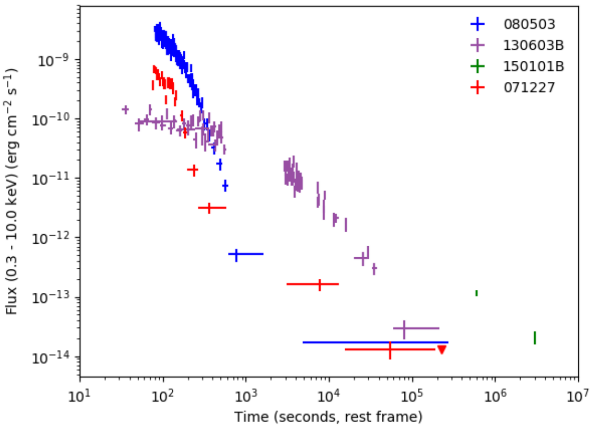

Figure 8. The available XRT or *Chandra* light curves for a subsample of SGRBs with kilonova candidates and GRB 071227. In the case of GRB 080503, we used the observed times.

We replotted the available XRT light curves for this subsample and compare them more directly with that of GRB 071227 in Fig. 8. As the XRT light curve for GRB 150101B is contaminated by an AGN, we have used the *Chandra X-ray Observatory* (*Chandra*) light curve from Fong et al. (2016). We find that GRB 071227 is again relatively underluminous at late times, while at early times is also dimmer than the well-sampled light curve of GRB 080503. However, GRB 071227 is not atypical for this subsample and is a strong behavioural match to GRB 080503. We have also plotted the light curves of the subsample of SGRBs with known redshift given in table 3 of D'Avanzo et al. (2014) normalized to their $E_{\gamma,\,\mathrm{iso}}$ as in fig. 2(b) of Troja et al. (2018), shown in our Fig. 9. We find, once again, that GRB 071227 is typical for this sample, although a lack of late time X-ray data means we cannot preclude the same behaviour found in GRB 150101B by Troja et al. There is also a clearer agreement between GRB 071227 and GRB 130603B at later times, although GRB 130603B has an early plateau not found in GRB 071227. This analysis of the X-ray agrees with the conclusion

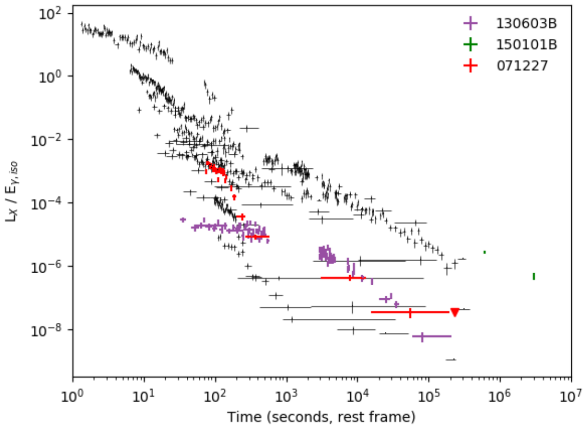

Figure 9. The available XRT or *Chandra* light curves normalized to their $E_{\gamma,\mathrm{iso}}$ for the subsample of SGRBs with known redshift given in D'Avanzo et al. (2014)'s table 3. We have highlighted the light curves of our kilonova candidate sample and GRB 071227.

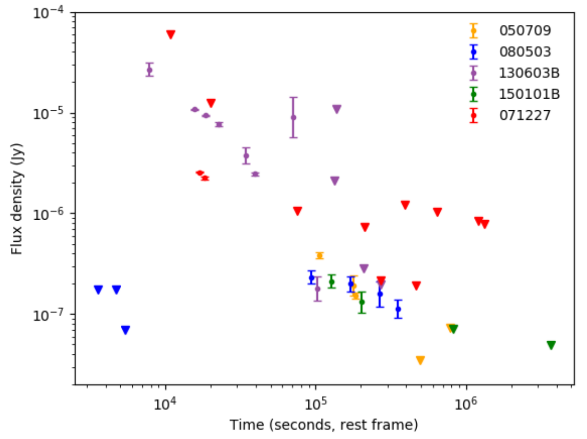

Figure 10. The available *r*/*R*-band light curves for our sample of kilonova candidates extrapolated to the same redshift as GRB 071227 without *k*-corrections and GRB 071227. We have applied an extinction of $E(B-V) = 0.43$ mag to the light curve for GRB 071227 as the other GRBs are little affected by extinction. In the case of GRB 080503, where no redshift could be identified, we use the observed times and magnitudes. The photometry is taken from Hjorth et al. (2005) and Jin et al. (2016); Perley et al. (2009); Cucchiara et al. (2013), de Ugarte Postigo et al. (2014) and Pandey et al. (2019); and Fong et al. (2016) for GRBs 050709, 080503, 130603B, and 150101B, respectively.

of Nicuesa Guelbenzu et al. (2014) that GRB 071227 is indeed an SGRB.

Several of our sample GRBs were also observed at optical wavelengths. In Fig. 10, we plot the available *r*/*R*-band light curves extrapolated to the same redshift as GRB 071227. It should be noted that GRB 130603B was assumed to be afterglow dominated at optical wavelengths and indications of a kilonova were identified in the NIR. We find that, while no strong conclusions can truly be drawn due to the poor sampling of the light curve, GRB 071227 is qualitatively similar to both GRB 050709 and GRB 150101B. In both these cases, the optical observations were used to infer the presence of a kilonova. We cannot preclude the possibility that GRB 071227 is also consistent with the behaviour exhibited by GRB 080503, where later brightening in the optical has been interpreted as a kilonova with a central engine (Metzger & Fernández 2014). However, the redshift of GRB 080503 is unknown and unlikely to be low. We also compare the light curve to the models of the AT 2017gfo emission in the same bands from Gompertz et al. (2018), as shown in Fig. 3, and find them to be generally inconsistent with GRB 071227. However, as the light-curve models are strictly phenomenological in regards to AT 2017gfo, this does not preclude other kilonova models being consistent with GRB 071227.

Unfortunately, although the light curves for our subsample of potential kilonovae are often better sampled than GRB 071227, there is a lack of multiband or spectroscopic observations. In particular, it is impossible to evaluate the SEDs of many of these other candidates in order to more directly compare with the transient identified here.

3.2.3 *Possible contributions from other afterglow mechanisms*

There are several other potential mechanisms which could contribute to producing an optical flash. These include a reverse shock passing through the shell as the outflow decelerates (Kobayashi & Sari 2000) or a hypothetical coupled optical and X-ray flare during the ∼1.1 d time period over which our X-ray spectrum was taken.

Short GRBs are typically described by the thin shell regime where the dimensionless parameter $\xi_0 > 1$ and a reverse shock is inefficient at slowing the shell down. To test if the excess emission at ∼0.26 d is the result of a reverse shock, we can estimate the expected flux from the reverse shock given the observed GRB parameters. The maximum flux and the characteristic frequency for the reverse shock are given by Harrison & Kobayashi (2013)

$$F_{\nu,\mathrm{max,R}} \sim F_{\nu,\mathrm{max,F}} C_\mathrm{F} \Gamma_0 R_B^{1/2} \quad (5)$$

and

$$\nu_{\mathrm{m,R}} \sim \nu_{\mathrm{m,F}} C_\mathrm{M} \Gamma_0^{-2} R_B^{1/2}, \quad (6)$$

where $F_{\nu,\mathrm{max}}$ is the maximum synchrotron flux and the subscript R or F indicates reverse and forward shock, respectively, Γ_0 is the bulk Lorentz factor of the outflow, C_F and C_M are correction factors, and R_B is a parameter that can be used to boost the magnetic equipartition value ε_B in the reverse shock region where magnetic fields from the central engine may still contribute.

Assuming an efficiency of $\eta = 0.1$ for the gamma-ray energy, the kinetic energy E_K of the blastwave is $\sim 1.8 \times 10^{51}$ erg. The dimensionless parameter for this burst is then $\xi_0 \approx (l/cT_{90})^{1/2}\Gamma_0^{-4/3}$ where $\Gamma_0 = 100$, the Sedov length is $l = (3E_\mathrm{K}/4\pi m_\mathrm{p} n c^2)^{1/3}$, $n \sim 10^{-3}$ is the ambient number density, and m_p is the mass of a proton. For these parameters, $\xi_0 \sim 24$ which confirms the thin nature of the shell. From Harrison & Kobayashi (2013), the correction factors are given by $C_\mathrm{F} \sim (1.5 + 5\xi_0^{-1.3})^{-1} \sim 0.6$ and $C_\mathrm{M} \sim 5 \times 10^{-3} + \xi_0^{-3} \sim 5 \times 10^{-3}$, and $F_{\nu,\mathrm{max},R} \sim 60 F_{\nu,\mathrm{max},F}$ and $\nu_{\mathrm{m},R} \sim 5 \times 10^{-3} \nu_{\mathrm{m},F}$. The characteristic frequency for the forward shock at the deceleration time, when the reverse shock peaks, is $\nu_{\mathrm{m},F} \sim 5.3 \times 10^{14}$ Hz where we assume $\varepsilon_B = 0.01$, $\varepsilon_\mathrm{e} = 0.1$, and $\Gamma_0 = 100$. This indicates that the forward shock in the optical frequencies will be $\sim F_{\nu,\mathrm{max},F}$ at peak, and the characteristic frequency for the reverse shock will be $\nu_{\mathrm{m},R} \sim 2.65 \times 10^8$ Hz. As $\nu_{\mathrm{m},R} < \nu$, the flux in the optical at the peak of the reverse shock is $F_\nu \sim F_{\nu,\mathrm{max},R}(\nu/\nu_{\mathrm{m},R})^{-(p-1)/2} \sim 4 \times 10^{-2} F_{\nu,\mathrm{max},F}$ and well below the level of the forward shock. Even for a very large R_B parameter the reverse shock will be only marginally brighter than the forward shock at deceleration and then decline rapidly as $t^{-(27p+7)/35}$ (Kobayashi 2000).

The peak of the afterglow at frequencies $\nu \geq \nu_\mathrm{m}$ is at the deceleration time, typically given by $t_\mathrm{d} \sim C_\mathrm{t} l/c\Gamma_0^{8/3}$, where $C_\mathrm{t} \sim$

0.2 is the correction factor for our parameters. For the outflow to decelerate at ∼0.26 d then the Lorentz factor for the outflow would be $\Gamma_0 \sim 20$; such a low Lorentz factor is inconsistent with a bright GRB (Lamb & Kobayashi 2016) and would reduce the reverse shock flux amplitude.

The causes of X-ray and optical flares in SGRBs are not yet understood but suggested mechanisms include fragmentation in the accretion disc surrounding the merger remnant and associated variation of the central engine (Perna, Armitage & Zhang 2006) or the fallback of material on eccentric orbits (Rosswog 2007). While a flare is unlikely to be a dominant factor in the X-ray spectrum over this period, a flare coinciding with our optical detections could potentially cause both the excess optical flux and steepness. However, there is the suggestion of corresponding features in both the X-ray and optical/NIR light curves of some events (e.g. Malesani et al. 2007; D'Avanzo 2015). In particular, Malesani et al. conclude that their optical observations following GRB 050724 are linked to a coincident X-ray flare, and that the rapid fading of their optical light curve is linked to the end of this flare. They do find the SED to be consistent between the X-ray and optical, which is not the case for GRB 071227 although, as previously mentioned, the long time period used to derive our X-ray spectrum could obscure a steepening in the X-ray at a coincident time to our optical detections. It should also be noted, however, that GRB 050724 was an unusual event and evidence for the coupling of optical and X-ray flares is scant.

GRB 071227 has previously been examined for X-ray flares by Margutti et al. (2011), and a potential flare was identified beginning at ∼150 s, concluding well before our spectral time period and much earlier than our optical detections. No further flares were identified by Margutti et al. and we find no evidence for one in the XRT light curve, a conclusion also reached by Bernardini et al. (2011). Despite this, the low X-ray count rate at later times means we cannot conclusively rule out an X-ray flare at a time when our optical data could be affected.

It is unlikely therefore that there is any significant contribution to our optical transient from these mechanisms.

3.3 GRB 071227 as an extended emission GRB

GRB 071227 has also been interpreted as an EE GRB (Norris, Gehrels & Scargle 2010; Lien et al. 2016; Gibson et al. 2017). With $T_{90} = 142.5 \pm 48.4$ s and $E_{\gamma,\mathrm{iso}} = 1.96^{+0.30}_{-0.29} \times 10^{50}$ erg in the *Swift*-BAT bandpass (*k*-corrected, cf. Bloom, Frail & Sari 2001), GRB 071227 is one of the longest but least energetic EE GRBs. However, the spread in durations and energies in the population is very limited (e.g. Gompertz et al. 2013); hence the large uncertainty on these measurements means it could be of more typical duration and energy. When corrected for redshift, $T_{90,\mathrm{rest}} = 102.9 \pm 34.9$ s, which is again both the longest of any EE burst but consistent within errors with being more typical. 29 per cent of the total energy release occurs within the first 2 s after trigger – one of the highest prompt-to-EE energy ratios in the sample.

One of the EE GRB sample, GRB 060614, contains a suspected kilonova (Xu et al. 2009; Yang et al. 2015). It should be noted that the classification of an EE GRB is still somewhat unclear and some studies take GRB 060614 to be a long burst (Gehrels et al. 2006; McBreen et al. 2008; Tanga et al. 2018). The EE of GRB 060614 contained a factor of ∼3 times more energy than GRB 071227, but the prompt spike energy was comparable between the two. The light curves of both GRBs are shown in Fig. 11. After the cessation of EE, the two bursts show markedly different afterglows. GRB 060614 exhibits a long X-ray plateau, symptomatic of energy injection into the emission site, while GRB 071227 appears to decay as a simple power law. However, due to the sparse data, an injection plateau similar to, but shorter than, GRB 060614 cannot be totally discounted. In the *r* band, GRB 060614 is almost an order of magnitude brighter than that observed in the first epoch of our observations of GRB 071227, with no extinction corrections applied. The light curve of GRB 060614 has been shown to be consistent with a synchrotron afterglow in which the peak frequency is passing through the *r* band (Gompertz et al. 2015). Similarly to GRB 071227, any possible thermal features at optical wavelengths are mostly masked by bright synchrotron emission. The difference in afterglow luminosity between the two bursts could be due to energy injection, as evidenced by the X-ray injection plateau in GRB 060614, or due to a denser circumburst environment around GRB 060614, which would result in a greater flux at both optical and X-ray frequencies. At the time of the F814W filter excess in GRB 060614 (Yang et al. 2015), the observations available for GRB 071227 are not very constraining; the 3σ upper limits in the *r* and *i* bands permit an optical afterglow or kilonova up to the luminosity of the one seen in GRB 060614.

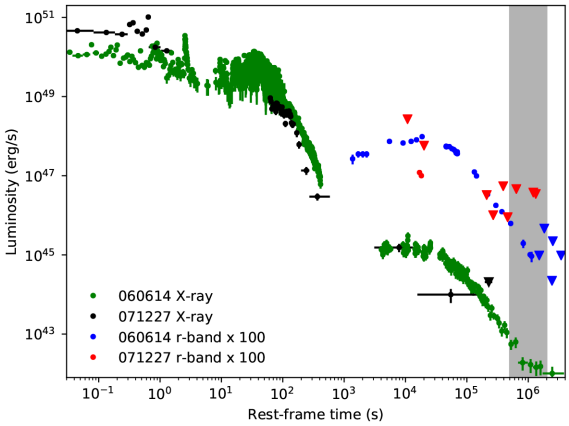

Figure 11. GRB 071227 versus GRB 060614, a short GRB with EE and a suspected kilonova. A composite BAT + XRT bolometric light curve is shown in black (green) for GRB 071227 (GRB 060614). The *r*-band light curve of GRB 071227 (GRB 060614) is plotted in red (blue). This has not been *k*-corrected, but the effect is small, and the optical light curves have also been shifted up by a factor of 100. The grey region marks the time of the excess in the F814W band that was claimed as a possible kilonova in GRB 060614 (Yang et al. 2015).

4 HOST GALAXY PROPERTIES

4.1 Host galaxy morphology and GRB offset

The host galaxy of GRB 071227 can be clearly identified as a late-type spiral with an observed optical disc radius of ∼20 kpc in both the data presented here, and in D'Avanzo et al. (2009) and Fong et al. (2013). The disc is viewed mostly edge on, with an inclination of ∼73° which we derive from fitting elliptical isophotes to our highest quality image, the second epoch *r*-band image. The host has a rest-frame *B*-band absolute magnitude of $M_B = -19.3$ (D'Avanzo et al. 2009). Fong & Berger (2013) examine the morphology of the galaxy and fit the surface brightness profile to a Sérsic model consistent with an exponential disc.

Leibler & Berger (2010), meanwhile, fit SEDs to optical and infrared observations of the host to identify its age and mass. Fitting to a single stellar population indicates an age of 0.49 Gyr and a

mass of 0.025×10^{12} $M_\odot$. A fit using only the *K*-band fluxes gave a maximum stellar mass of 0.25×10^{12} $M_\odot$.

Radio observations of the host have also been performed (Nicuesa Guelbenzu et al. 2014), detecting a total integrated flux density of $F_\nu = 43 \pm 11$ μJy at 5.5 GHz. While the centre of the radio emission is offset from the galactic bulge visible in the optical, this is deemed insignificant and within error bounds. Nicuesa Guelbenzu et al. conclude that the galaxy is inactive, due to its position on a *WISE* 3.4–4.6–12 μm (W1–W2–W3) colour–colour plot (using Vega magnitudes) and morphology at 5.5 GHz. This colour–colour plot indicates the host to be an LIRG (luminous infrared galaxy). SED fitting with additional data from Leibler & Berger (2010) and the *WISE* survey indicates a stellar mass of 0.32×10^{12} $M_\odot$.

We used the position of the transient identified from our subtractions to measure an offset of 2.91 ± 0.10 arcsec from the Galactic Centre. At $z = 0.381$, this corresponds to 15.71 ± 0.54 kpc, consistent with the ∼15 kpc offsets found by D'Avanzo et al. and Fong & Berger.

4.2 Spatially resolved emission line spectroscopy

The 11 subspectra extracted from our GMOS-S spectroscopy were separately analysed to determine spatially resolved properties of the stars and gas across the host galaxy, although it should be noted that the subspectra are not truly independent. As well as analysing the individual subspectra we split the galaxy into two disc sections (subspectra 1–4 and 8–11) and a central region (subspectra 5–7) in order to increase the signal-to-noise ratio (SNR) of the spectra being analysed. Fig. 2 demonstrates this. This analysis was done following the procedure explained in Lyman et al. (2018). Briefly, the stellar continuum was fit using STARLIGHT (Cid Fernandes et al. 2005) and the resulting emission-line spectrum (after subtraction of this stellar continuum model) was fit with a series of Gaussians centred at locations of strong nebular lines. The emission line ratios and fluxes were used to derive properties such as extinction, via the Balmer decrement, and metallicity, using indicators from Pettini & Pagel (2004).

Many of the individual subspectra had too low SNR in order to robustly fit either the stellar continuum or the nebular lines. Even with binning of the subspectra, the SNR was not sufficient to tightly constrain the fit of the stellar continuum, which are notoriously prone to multiple degeneracies and prove problematic to interpret even in high SNR data. For the nucleus, where the continuum signal is strongest, we find the best-fitting stellar population model to be dominated by an old stellar population at $\gtrsim$10 Gyr with a modest (few per cent by mass) contribution from younger populations at $\lesssim$1 Gyr. This is somewhat consistent with the young+old simple stellar population model used by Leibler & Berger (2010), a model fitted to the galaxy's observed SED in which the stellar population is divided into old stars with an age identical to that of the Universe at the host's redshift, and a more recently formed stellar population with a fitted age of 0.36 Gyr. They inferred stellar masses of $<0.100 \times 10^{12}$ $M_\odot$ for the old population and 0.020×10^{12} $M_\odot$ for the young.

At the location of the GRB (subspectrum 2), our emission line fits gave $E(B-V)_{\rm gas} = 0.54 \pm 0.37$ mag of extinction based on the Balmer decrement, assuming an intrinsic $F(\mathrm{H}\,\alpha)/F(\mathrm{H}\,\beta) = 2.86$ (Osterbrock & Ferland 2006), as expected from our spectral fits of GRB 071227. When analysing the combined disc spectrum from subspectra 1–4 to obtain a higher SNR in the lines, we obtain $E(B-V)_{\rm gas} = 0.53 \pm 0.16$ mag, greater extinction than identified in many other SGRB hosts examined (Savaglio, Glazebrook & Le Borgne 2009; Yoshida et al. 2019). The metallicity at the GRB location was found to be $12 + \log(\mathrm{O/H}) = 8.5 \pm 0.3$ and 8.5 ± 0.2 dex, using the N2 and O3N2 relations of Pettini & Pagel (2004), respectively. When considering the summed disc spectrum on the GRB side of the galaxy, these values are 8.7 ± 0.1 and 8.6 ± 0.1 dex, respectively. These are consistent with the range of 8.2–8.8 inferred by D'Avanzo et al. (2009) for this host, and are also comparable to the sample of local galaxies (∼7.5–9.2; Walter et al. 2008) and the Milky Way (∼8.7; Baumgartner & Mushotzky 2006). Of particular note is the similarity to the metallicity inferred for the host of SGRB 080905A (∼8.4–8.8; Rowlinson et al. 2010). Note that these gas-phase metallicities are relevant only for the ongoing star formation and young stellar population of the host, and thus may not be indicative of the metallicity of a possible very old progenitor. When analysing the disc on the opposite side of the nucleus from the GRB, we find very similar metallicity values but a somewhat higher $E(B-V)_{\rm gas} \sim 1.4$ mag. The difference in extinction on opposing sides of the disc may be a result of viewing the host edge on and the geometry of the dust lanes with respect to the spiral arms.

We measure a total host unobscured [O II] luminosity of $\sim 5 \times 10^{40}$ erg s^{-1}, which, using equation 3 from Kennicutt (1998), gives a star formation rate of 0.7 ± 0.2 $M_\odot$ yr^{-1}. Alternatively, using equation 10 from Kewley, Geller & Jansen (2004) and our mean metallicity of 8.6, gives a rate of $0.2^{+0.4}_{-0.2}$ $M_\odot$ yr^{-1}. D'Avanzo et al. (2009) used their [O II] luminosity of 3.9×10^{40} erg s^{-1} to identify a star formation rate of 0.6 $M_\odot$ yr^{-1}, consistent with our calculations. Returning to the radio observations performed by Nicuesa Guelbenzu et al. (2014), a fit using the GRASIL software indicates a star formation rate of 24 $M_\odot$ yr^{-1} implying the host is undergoing an intensive star-forming period, however. The discrepancy with the optical emission line diagnostics is attributed to large amounts of optically obscured star formation by Nicuesa Guelbenzu et al. (2014).

4.3 Rotation curve

The nearly edge-on orientation of the host galaxy gives us an excellent view on the rotation curve of the galaxy. In the 2D spectrum a clear slant can be seen in the [S II], H α, [N II], [O III], H β, and [O II] lines. To determine the rotation curve of the galaxy we used the NGAUSSFIT routines in the IRAF STSDAS package. We extracted postage stamp spectra using a 5 pixels bin in the spatial direction (corresponding to 0.73 arcsec or 3.79 kpc) and 150 pixels in the dispersion direction from the 2D spectra. We then fitted the continuum level and slope, and fitted the line with a Gaussian profile to determine its centre position. The postage stamps were shifted with 3 pixels in spatial direction after each fit. This minimizes the effect of weak cosmic rays and residuals of skylines, but also results in non-independent data points.

The H α line is bright, but the Balmer stellar atmospheric absorption is strong near the nucleus; we did not explicitly fit for the absorption in the line centroid measurements.

The [O II] doublet is not as bright as the H α line, but the local continuum is extremely weak, making the line centre easy to fit, although it is more difficult to determine the galaxy centre pixel. Furthermore, the H α and [O II] lines are located at the extreme ends of the spectrum, where the arc spectrum has only a few lines, making the wavelength calibration less certain. We therefore also fitted the [N II], [O III], and H β lines, but did not use the [S II] doublet which is too close to the end of the chip. The resulting radial velocity measurements, including only points with a velocity uncertainty better than 100 km s^{-1}, are shown in Fig. 12. The GRB took place in the approaching, south-east, end of the galaxy as indicated.

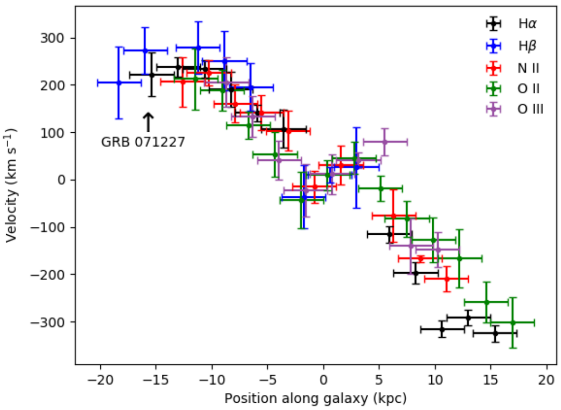

Figure 12. The rotation curve of the host galaxy, velocities are as observed (not corrected for the inclination). The position of the GRB in the south-east tip of the galaxy moving away from us is noted.

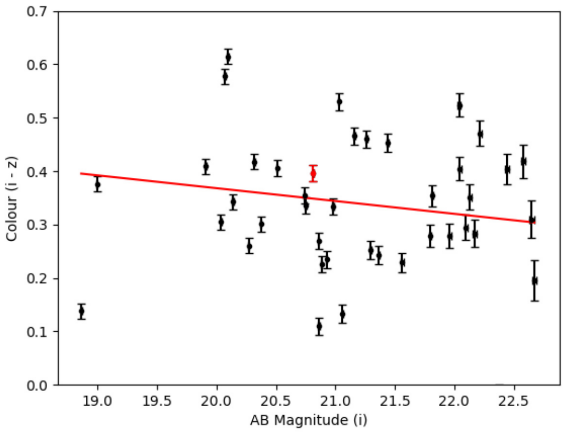

Figure 13. A colour–magnitude plot and the expected red sequence at $z = 0.381$ (red, solid) for the *i*/*z* filter combination. The host of GRB 071227 is highlighted in red.

The rotation curve appears to consist of a disc-like profile with a significant undulation around the centre, particularly clear in [O II], [O III], and [N II]. This undulation is possibly caused by a centrally located bar structure, a large spiral arm or a counterrotating disc, but to establish this definitively, a much higher signal to noise is required so the line centres can be measured in smaller bins and the zero position and velocity can be more accurately determined. We can, however, estimate the dynamical mass of the galaxy through the velocity at which the rotation curve levels off, which we evaluate by using a weighted mean of a rebinned data set, using inverse variance weighting taking into account the bin overlap. Following their initial kicks, the mass of their host is an important parameter in the travel of a compact binary. Identifying the host's mass therefore is useful for understanding and constraining the potential offsets of SGRBs from their hosts, which could enable host associations and therefore redshifts in other SGRBs. We correct for the inclination of $\sim 73^{\circ}$ as identified in Section 4.1, and find a dynamical mass of $\sim 0.32 \times 10^{12}$ $M_{\odot}$, consistent with the stellar masses of 0.32×10^{12} $M_{\odot}$ found by Nicuesa Guelbenzu et al. (2014) and 0.25×10^{12} $M_{\odot}$ found by Leibler & Berger (2010), an agreement typical for galaxies of this mass (Drory, Bender & Hopp 2004). This mass is approximately 20–30 per cent of that inferred for the Milky Way (McMillan 2017) and an order of magnitude larger than that of the host of GRB 080905A (Rowlinson et al. 2010).

4.4 Host environment

The evolution of a galaxy, and by extension, the objects within, can be strongly influenced by its environment. It is therefore important to identify key features of a host galaxy's environment, such as clustering, to better inform future observations of GRBs. In addition, determining the relationship between SGRB hosts and their environments could allow redshifts to be inferred for hostless SGRBs.

Whilst it appears from our imaging data that the host of GRB 071227 is in a local cluster, we can verify this assertion using red sequencing: a colour–magnitude plot of the galaxies within a cluster will display a linear relationship known as the red sequence, the specifics of which are defined by the redshift of the cluster (Gladders & Yee 2000). We produced a plot of the colour–magnitude relation for each combination of filters for the galaxies visible within the GMOS-S field, an example of which is shown in Fig. 13, including the expected red sequences at our redshift of 0.381, which we constructed using the Millenium *N*-body simulation (Springel et al. 2005) and a similar methodology to Stott et al. (2009). The galaxy evolution in our case is defined in Lagos et al. (2012). Our red sequences consistently indicate that the host of GRB 071227, marked in red in the plots, is indeed part of a local cluster of galaxies.

5 CONCLUSIONS

We have investigated the short duration GRB 071227 at X-ray and optical wavelengths, and find apparent excess optical flux inconsistent with the inferred afterglow extrapolated from fitting only the X-ray data. Using an MCMC method to fit the SED, however, we find that both the X-ray and optical transients are generally consistent with an afterglow where $\Gamma \sim 2.1$–2.2, although an excess remains in the z band.

We also investigate other possible causes of this excess. We find that fitting the excess to a blackbody is generally inconsistent with the results expected from kilonova models, requiring superluminal motion and a high ejecta mass of ~ 0.1 $M_{\odot}$, and varying the afterglow parameters and extinction generally fails to reconcile this. We cannot fully rule out some thermal contribution, however, which could be responsible for the z-band excess. Additionally, we have compared GRB 071227 to several kilonova candidates, finding the *r*/*R*-band and XRT light curves of GRB 071227 to be consistent with these observations and with the sample of SGRBs in general.

We find the excess is also inconsistent with being the result of a reverse shock and there is no evidence for a coupled X-ray optical flare as has been previously suggested in the case of GRB 050724. We have examined GRB 071227 in the context of EE GRBs, particularly in comparison to GRB 060614.

Finally, we have performed spectroscopic analysis of the host of GRB 071227. We find that the host is a spiral galaxy with a dynamical mass of $\sim 0.35 \times 10^{12}$ $M_{\odot}$. In addition, we have derived a majority stellar population age of $\gtrsim 10$ Gyr with a small contribution from a younger population, a mean metallicity of $12 + \log(\mathrm{O/H}) = 8.6$ dex and a star formation rate of 0.2–0.7 $M_{\odot}$ yr^{-1}. We evaluate the extinction of the galaxy finding it to be dustier than many other SGRB hosts with $E(B-V)_{\mathrm{gas}} = 0.54 \pm 0.37$ near the GRB and $E(B-V)_{\mathrm{gas}} \sim 1.4$ in the other disc region. We also used red sequencing to show that the galaxy is situated in a local cluster. Overall, despite having a higher intrinsic extinction than most other examples, we find the host of GRB 071227 to be a typical late-type SGRB host, less massive and with comparable metallicity to the Milky Way.

ACKNOWLEDGEMENTS

Based on observations obtained at the Gemini Observatory, which is operated by the Association of Universities for Research in Astronomy, Inc., under a cooperative agreement with the NSF on behalf of the Gemini partnership: the National Science Foundation (United States), the National Research Council (Canada), CONICYT (Chile), Ministerio de Ciencia, Tecnología e Innovación Productiva (Argentina), and Ministério da Ciência, Tecnologia e Inovação (Brazil) (acquired through the Gemini Observatory Archive and processed using the Gemini IRAF package).

This research has made use of the services of the ESO Science Archive Facility. Based on observations collected at the European Southern Observatory under ESO programme 080.D-0906(G).

This work made use of data supplied by the UK *Swift* Science Data Centre at the University of Leicester.

The national facility capability for SkyMapper has been funded through ARC LIEF grant LE130100104 from the Australian Research Council, awarded to the University of Sydney, the Australian National University, Swinburne University of Technology, the University of Queensland, the University of Western Australia, the University of Melbourne, Curtin University of Technology, Monash University, and the Australian Astronomical Observatory. SkyMapper is owned and operated by The Australian National University's Research School of Astronomy and Astrophysics. The survey data were processed and provided by the SkyMapper Team at ANU. The SkyMapper node of the All-Sky Virtual Observatory (ASVO) is hosted at the National Computational Infrastructure (NCI). Development and support the SkyMapper node of the ASVO has been funded in part by Astronomy Australia Limited (AAL) and the Australian Government through the Commonwealth's Education Investment Fund (EIF) and National Collaborative Research Infrastructure Strategy (NCRIS), particularly the National eResearch Collaboration Tools and Resources (NeCTAR) and the Australian National Data Service Projects (ANDS).

RAJE, PTO, RLCS, GPL, and NRT acknowledge funding from the Science and Technology Facilities Council.

KW and BPG have received funding from the European Research Council (ERC) under the European Union's Horizon 2020 research and innovation programme (grant agreement no 725246, TEDE, PI Levan).

SR has been supported by the Swedish Research Council (VR) under grant number 2016-03657 3, by the Swedish National Space Board under grant number Dnr. 107/16 and by the research environment grant 'Gravitational Radiation and Electromagnetic Astrophysical Transients' (GREAT) funded by the Swedish Research council (VR) under Dnr. 2016-06012. Support from the COST Actions on neutron stars (PHAROS; CA16214) and black holes and gravitational waves (GWerse; CA16104) are gratefully acknowledged.

The authors would like to thank Andy Fruchter and John Graham for their contributions to the Gemini South observations. We also thank Brian Metzger and Masaomi Tanaka for helpful discussion and suggestions. Finally, we thank the anonymous referee for their useful comments.

REFERENCES

Abbott B. P. et al., 2017, ApJ, 848,
Alard C., 2000, A&AS, 144, 363
Arnaud K. A., 1996, in Jacoby G. H., Barnes J., eds, ASP Conf. Ser. Vol. 101, Astronomical Data Analysis Software and Systems V. Astron. Soc. Pac., San Francisco, p. 17
Ascenzi S. et al., 2019, MNRAS, 486, 672
Barnes J., Kasen D., Wu M.-R., Martínez-Pinedo G., 2016, ApJ, 829, 110
Baumgartner W. H., Mushotzky R. F., 2006, ApJ, 639, 929
Beardmore A. P., Page K. L., Sakamoto T., 2007, GCN Circ., 7153, 1
Becker A., 2015, Astrophysics Source Code Library, record ascl:1504.004
Berger E., Morrell N., Roth M., 2007, GCN Circ., 7151, 1
Bernardini M. G., Margutti R., Chincarini G., Guidorzi C., Mao J., 2011, A&A, 526, A27
Bertin E., Arnouts S., 1996, A&AS, 117, 393
Bloom J. S., Frail D. A., Sari R., 2001, AJ, 121, 2879
Brege W. et al., 2018, Phys. Rev. D, 98, 063009
Cardelli J. A., Clayton G. C., Mathis J. S., 1989, ApJ, 345, 245
Chevalier R. A., Li Z.-Y., 1999, ApJ, 520, L29
Chevalier R. A., Li Z.-Y., 2000, ApJ, 536, 195
Cid Fernandes R., Mateus A., Sodré L., Stasińska G., Gomes J. M., 2005, MNRAS, 358, 363
Covino S. et al., 2017, Nat. Astron., 1, 791
Cowperthwaite P. S. et al., 2017, ApJ, 848, L17
Cucchiara A. et al., 2013, ApJ, 777, 94
D'Avanzo P., 2015, J. High Energy Astrophys., 7, 73
D'Avanzo P. et al., 2007, GCN Circ., 7149, 1
D'Avanzo P. et al., 2009, A&A, 498, 711
D'Avanzo P. et al., 2014, MNRAS, 442, 2342
de Ugarte Postigo A. et al., 2014, A&A, 563, A62
Dorman B., Arnaud K. A., 2001, in Harnden F. R., Jr, Primini F. A., Payne H. E., eds, ASP Conf. Ser. Vol. 238, Astronomical Data Analysis Software and Systems X. Astron. Soc. Pac., San Francisco, p. 415
Draper P. W., Gray N., Berry D. S., Taylor M., 2014, Astrophysics Source Code Library, record ascl:1403.024
Drory N., Bender R., Hopp U., 2004, ApJ, 616, L103
Duffell P. C., Quataert E., Kasen D., Klion H., 2018, ApJ, 866, 3
Duflo J., Zuker A. P., 1995, Phys. Rev. C, 52, R23
ESO, 2018, FORS2 User Manual issue 104; VLT-MAN-ESO-13100-1543. European Southern Observatory.
Evans P. A. et al., 2007, A&A, 469, 379
Evans P. A. et al., 2009, MNRAS, 397, 1177
Fong W., Berger E., 2013, ApJ, 776, 18
Fong W. et al., 2013, ApJ, 769, 56
Fong W., Berger E., Margutti R., Zauderer B. A., 2015, ApJ, 815, 102
Fong W. et al., 2016, ApJ, 833, 151
Foucart F. et al., 2014, Phys. Rev. D, 90, 024026
Foucart F., Duez M. D., Kidder L. E., Nissanke S., Pfeiffer H. P., Scheel M. A., 2019, Phys. Rev. D, 99, 103025
Fox D. B. et al., 2005, Nature, 437, 845
Freudling W., Romaniello M., Bramich D. M., Ballester P., Forchi V., García-Dabló C. E., Moehler S., Neeser M. J., 2013, A&A, 559, A96
Fukugita M., Ichikawa T., Gunn J. E., Doi M., Shimasaku K., Schneider D. P., 1996, AJ, 111, 1748
Gehrels N. et al., 2006, Nature, 444, 1044
Gibson S. L., Wynn G. A., Gompertz B. P., O'Brien P. T., 2017, MNRAS, 470, 4925
Gladders M. D., Yee H. K. C., 2000, AJ, 120, 2148
Glazebrook K., Bland-Hawthorn J., 2001, PASP, 113, 197
Goldstein A. et al., 2017, ApJ, 848, L14
Gompertz B. P., O'Brien P. T., Wynn G. A., 2014, MNRAS, 438, 240
Gompertz B. P., O'Brien P. T., Wynn G. A., Rowlinson A., 2013, MNRAS, 431, 1745
Gompertz B. P., van der Horst A. J., O'Brien P. T., Wynn G. A., Wiersema K., 2015, MNRAS, 448, 629
Gompertz B. P. et al., 2018, ApJ, 860, 62
Granot J., Sari R., 2002, ApJ, 568, 820
Güver T., Özel F., 2009, MNRAS, 400, 2050
Hamuy M., Walker A. R., Suntzeff N. B., Gigoux P., Heathcote S. R., Phillips M. M., 1992, PASP, 104, 533
Hamuy M., Suntzeff N. B., Heathcote S. R., Walker A. R., Gigoux P., Phillips M. M., 1994, PASP, 106, 566
Harrison R., Kobayashi S., 2013, ApJ, 772, 101

Hjorth J. et al., 2003, Nature, 423, 847
Hjorth J. et al., 2005, Nature, 437, 859
Hook I. M., Jørgensen I., Allington-Smith J. R., Davies R. L., Metcalfe N., Murowinski R. G., Crampton D., 2004, PASP, 116, 425
Jin Z.-P. et al., 2016, Nat. Commun., 7, 12898
Jin Z.-P., Covino S., Liao N.-H., Li X., D'Avanzo P., Fan Y.-Z., Wei D.-M., 2019, preprint (arXiv:1901.06269)
Kasen D., Fernández R., Metzger B. D., 2015, MNRAS, 450, 1777
Kasliwal M. M. et al., 2017, Science, 358, 1559
Kennicutt Jr. R. C., 1998, ARA&A, 36, 189
Kewley L. J., Geller M. J., Jansen R. A., 2004, AJ, 127, 2002
Kilpatrick C. D. et al., 2017, Science, 358, 1583
Kisaka S., Ioka K., Sakamoto T., 2017, ApJ, 846, 142
Kobayashi S., 2000, ApJ, 545, 807
Kobayashi S., Sari R., 2000, ApJ, 542, 819
Korobkin O., Rosswog S., Arcones A., Winteler C., 2012, MNRAS, 426, 1940
Kouveliotou C., Meegan C. A., Fishman G. J., Bhat N. P., Briggs M. S., Koshut T. M., Paciesas W. S., Pendleton G. N., 1993, ApJ, 413, L101
Lagos C. d. P., Bayet E., Baugh C. M., Lacey C. G., Bell T. A., Fanidakis N., Geach J. E., 2012, MNRAS, 426, 2142
Lamb G. P., Kobayashi S., 2016, ApJ, 829, 112
Lamb G. P. et al., 2019, preprint (arXiv:1905.02159)
Lattimer J. M., Schramm D. N., 1974, ApJ, 192, L145
Leibler C. N., Berger E., 2010, ApJ, 725, 1202
Li Y., Li A., Wei D. M., 2008a, ApJ, 678, 1136
Li A., Liang S. L., Kann D. A., Wei D. M., Klose S., Wang Y. J., 2008b, ApJ, 685, 1046
Li L.-X., Paczyński B., 1998, ApJ, 507, L59
Lien A. et al., 2016, ApJ, 829, 7
Lyman J. D. et al., 2018, MNRAS, 473, 1359
Malesani D. et al., 2007, A&A, 473, 77
Mannucci F., Salvaterra R., Campisi M. A., 2011, MNRAS, 414, 1263
Margutti R. et al., 2011, MNRAS, 417, 2144
McBreen S. et al., 2008, ApJ, 677, L85
McMillan P. J., 2017, MNRAS, 465, 76
Metzger B. D., 2017, Living Rev. Relativ., 20, 3
Metzger B. D., Fernández R., 2014, MNRAS, 441, 3444
Metzger B. D., Piro A. L., 2014, MNRAS, 439, 3916
Metzger B. D., Bauswein A., Goriely S., Kasen D., 2015, MNRAS, 446, 1115
Möller P., Nix J. R., Myers W. D., Swiatecki W. J., 1995, At. Data Nucl. Data Tables, 59, 185
Nicuesa Guelbenzu A. et al., 2012, A&A, 548, A101
Nicuesa Guelbenzu A. et al., 2014, ApJ, 789, 45
Norris J. P., Gehrels N., Scargle J. D., 2010, ApJ, 717, 411
Osterbrock D. E., Ferland G. J., 2006, Astrophysics of Gaseous Nebulae and Active Galactic Nuclei, University Science Books, Sausalito, CA, USA
Pandey S. B. et al., 2019, MNRAS, 485, 5294
Pei Y. C., 1992, ApJ, 395, 130
Perley D. A. et al., 2009, ApJ, 696, 1871
Perna R., Armitage P. J., Zhang B., 2006, ApJ, 636, L29
Pettini M., Pagel B. E. J., 2004, MNRAS, 348, L59
Piran T., 2004, Rev. Mod. Phys., 76, 1143
Rieke G. H., Lebofsky M. J., 1985, ApJ, 288, 618
Rossi A. et al., 2019, preprint (arXiv:1901.05792)
Rosswog S., 2005, ApJ, 634, 1202
Rosswog S., 2007, MNRAS, 376, L48
Rosswog S., 2015, Int. J. Mod. Phys. D, 24, 1530012
Rosswog S., Feindt U., Korobkin O., Wu M.-R., Sollerman J., Goobar A., Martinez-Pinedo G., 2017, Class. Quantum Gravity, 34, 104001
Rowlinson A. et al., 2010, MNRAS, 408, 383
Sakamoto T. et al., 2007a, GCN Circ., 7147, 1
Sakamoto T., Norris J., Ukwatta T., Barthelmy S. D., Gehrels N., Stamatikos M., 2007b, GCN Circ., 7156, 1
Sari R., Piran T., 1999, ApJ, 520, 641
Sari R., Piran T., Narayan R., 1998, ApJ, 497, L17
Sari R., Piran T., Halpern J. P., 1999, ApJ, 519, L17
Savaglio S., Glazebrook K., Le Borgne D., 2009, ApJ, 691, 182
Savchenko V. et al., 2017, ApJ, 848, L15
Schlegel D. J., Finkbeiner D. P., Davis M., 1998, ApJ, 500, 525
Shaw R. A., 2016, GMOS Data Reduction Cookbook. http://ast.noao.edu/sites/default/files/GMOS_Cookbook/
Smartt S. J. et al., 2017, Nature, 551, 75
Springel V. et al., 2005, Nature, 435, 629
Stott J. P., Pimbblet K. A., Edge A. C., Smith G. P., Wardlow J. L., 2009, MNRAS, 394, 2098
Svensson K. M., Levan A. J., Tanvir N. R., Fruchter A. S., Strolger L. G., 2010, MNRAS, 405, 57
Tanga M., Krühler T., Schady P., Klose S., Graham J. F., Greiner J., Kann D. A., Nardini M., 2018, A&A, 615, A136
Tanvir N. R., Levan A. J., Fruchter A. S., Hjorth J., Hounsell R. A., Wiersema K., Tunnicliffe R. L., 2013, Nature, 500, 547
Tanvir N. R. et al., 2017, ApJ, 848, L27
Troja E. et al., 2018, Nat. Commun., 9, 4089
Troja E. et al., 2019, preprint (arXiv:1905.01290)
Walter F., Brinks E., de Blok W. J. G., Bigiel F., Kennicutt R. C., Thornley M. D., Leroy A., 2008, AJ, 136, 2563
Willingale R., Starling R. L. C., Beardmore A. P., Tanvir N. R., O'Brien P. T., 2013, MNRAS, 431, 394
Wilms J., Allen A., McCray R., 2000, ApJ, 542, 914
Wolf C. et al., 2018, Publ. Astron. Soc. Aust., 35, e010
Xu D. et al., 2009, ApJ, 696, 971
Yang B. et al., 2015, Nat. Commun., 6, 7323
Yoshida K., Yonetoku D., Arimoto M., Sawano T., Kagawa Y., 2019, PASJ, 71, 54

APPENDIX A: SPECTRAL ENERGY DISTRIBUTION (SED) FITS

Table A1. Our XSPEC fit to the X-ray spectrum using the absorbed power-law model `tbabs*ztbabs(powerlaw)`. This model represents a power-law spectrum, where flux density $A(E) = KE^{-\Gamma}$ for some energy E, Γ is the photon index, with $\Gamma = \beta + 1$, and K is the flux density at 1 keV. `Tbabs` and `ztbabs` apply interstellar medium (ISM) absorption corrections to the X-ray, with `tbabs` correcting for the Milky Way and `ztbabs` correcting for the host and its redshift (Wilms, Allen & McCray 2000). All errors are given to 90 per cent confidence limits.

Model component	Parameter	Value	Free parameter?
`TBabs`	N_H	1.3×10^{20} cm^{-2}	N
`zTBabs`	N_H	$\leq 2.94 \times 10^{21}$ cm^{-2}	Y
`zTBabs`	z	0.381	N
`powerlaw`	Γ	$1.58^{+0.87}_{-0.57}$	Y
`powerlaw`	K	$4.81^{+4.43}_{-1.75} \times 10^{-6}$ photons keV^{-1} cm^{-2} s^{-1}	Y

Table A2. Our XSPEC fit to the first epoch Gemini optical data using the absorbed power-law model `redden*zdust(powerlaw)`, where `redden` introduces a correction for IR/optical/UV extinction in the Milky Way (Cardelli et al. 1989) while `zdust` corrects for dust extinction in the host, again including its redshift (Pei 1992). Note that the `method` selected uses the extinction curves derived from the Milky Way. All errors are given to 90 per cent confidence limits.

Model component	Parameter	Value	Free parameter?
`redden`	$E(B-V)$	0.013	N
`zdust`	`method`	1	N
`zdust`	$E(B-V)$	0.00	N
`zdust`	R_v	3.08	N
`zdust`	z	0.381	N
`powerlaw`	Γ	$\leq$4.49	Y
`powerlaw`	K	$4.93^{+1.56\times10^{4}}_{-4.93} \times 10^{-13}$ photons keV^{-1} cm^{-2} s^{-1}	Y

Table A3. Our XSPEC fit to the combined X-ray and optical SED using the absorbed power-law model `redden*tbabs(zdust*ztbabs(powerlaw))`. As the normalization of the power law was allowed to vary between the X-ray and optical data, we list both below. All errors are given to 90 per cent confidence limits.

Model component	Parameter	Value	Free parameter?
`redden`	$E(B-V)$	0.013	N
`TBabs`	N_H	1.3×10^{20} cm^{-2}	N
`zdust`	`method`	1	N
`zdust`	$E(B-V)$	$\leq$0.85	Y
`zdust`	R_v	3.08	N
`zdust`	z	0.381	N
`zTBabs`	N_H	$\leq 8.22 \times 10^{21}$ cm^{-2}	Y
`zTBabs`	z	0.381	N
`powerlaw`	Γ	$1.58^{+0.56}_{-0.57}$	Y
`powerlaw`	$K_{\text{X-ray}}$	$4.81^{+2.13}_{-1.75} \times 10^{-6}$ keV^{-1} cm^{-2} s^{-1}	Y
`powerlaw`	K_{Optical}	$\leq 6.69 \times 10^{-4}$ photons keV^{-1} cm^{-2} s^{-1}	Y

Table A4. Our Markov Chain Monte Carlo (MCMC) power-law fit to the afterglow defined as $A(E) = KE^{-\Gamma}$ for some energy E as above. $E(B-V)$ is derived from the N_H using the relation identified by Güver & Özel (2009). All errors below are 1σ.

Parameter	Value
Γ	$2.19^{+0.06}_{-0.04}$
K	$4.12^{0.94}_{-1.05} \times 10^{-6}$ photons keV^{-1} cm^{-2} s^{-1}
N_H	$2.97^{+0.01}_{-0.64} \times 10^{21}$ cm^{-2}
$E(B-V)$	$0.43^{+0.01}_{-0.09}$ mag

Table A5. Our MCMC power-law fit to the afterglow where $E(B-V)$ is not linked explicitly to the N_H and all parameters are free to vary. All errors below are 1σ.

Parameter	Value
Γ	$2.15^{+0.01}_{-0.06}$
K	$5.80^{+1.70}_{-0.04} \times 10^{-6}$ photons keV^{-1} cm^{-2} s^{-1}
N_H	$2.77^{+5.51}_{-2.77} \times 10^{20}$ cm^{-2}
$E(B-V)$	$0.45^{+0.01}_{-0.07}$ mag

This paper has been typeset from a TEX/LATEX file prepared by the author.